Contents

Supplementary Note 1: Details of Bands along the x and y direction

Firstly, we illuminate that the coupling t_c has negligible influences to the transport properties and the band structures for a ribbon along the x direction. As shown in Figs. S1(a)-(b), The surface states' chirality holds for $t_c \neq 0$. Generally, it is attributed to the absent of the networks for the x-y and x-z surfaces states. The quantized transport properties are robust against disorder and are independent of t_c, as plotted in Figs. S1(c)-(d).

As a comparison, the bands along the y direction are obviously t_c-dependent. As shown in Fig. S4(g), the backscattering free chiral modes can be gapped out by turning on t_c, and the gaps are determined by t_c. These features are consistent with the transport properties in the main text. Generally, the gapped red chiral modes along k_y can be understood as follows:

(i) For $t_c = 0$, the red and blue chiral modes are decoupled, where their Fermi surfaces satisfy the plots in Fig. S4(d).

(ii) After turning on $t_c \neq 0$, the Fermi surfaces of the isolated front and back surfaces varies from the solid lines to the dashed lines as plotted in Figs. S4(b)-(c). Nevertheless, the dashed and solid lines are both topological nontrivial in the Brillouin zone. Since they both can not continuous deformed into a point, the dashed and solid lines both traversal the entire $k_{y/z} \in [0, 2\pi]$. It indicate that the number of chiral modes along the y direction is t_c independent for the isolated y-z surfaces. In other words, the chiral modes can not be gapped out for the isolated y-z surfaces.

(iii) In real systems, the required isolated y-z surfaces are not available for the considered sample. For example, the chiral turning on the top/bottom surfaces leads to an effective coupling between the front and back surfaces. Putting the two Fermi-surfaces together (see Fig. S4(e)) and considering their effective coupling, the intersection of the two Fermi surfaces should be released. Then, the Fermi surfaces in Fig. S4(e) will modified into Fig. S4(f), where a closed and topologically trivial Fermi surfaces are obtained.

(vi) Considering the colored regions between the Fermi surfaces, these momentums are unavailable for the chiral modes. Thus, for a particular Fermi energy E, the number of chiral modes along k_y should decrease accordingly.

(v) By increasing t_c, the colored regions should increase. Therefore, the number of chiral modes decreases by increasing t_c. These features are consistent with the band structures in Fig. S4(g).

Supplementary Note 2: Robust and quantized $G_x^{(xz)}+G_y^{(xy)}$

We present more details of the robustness and the quantized $G_x^{(xz)}+G_y^{(xy)}$ In theory, the quantized response $G_x^{(xz)}+G_y^{(xy)} = (L_y+L_z)e^2/h$ can be understood as follows.

First of all, when $G_y^{(xy)}$ deviates from its ideal value $L_z e^2/h$, there are $(L_z e^2/h - G_y^{(xy)})/(e^2/h)$ red backscattering channels follow the localized trajectory in Fig. S3(b). Significantly, the localized trajectory is available when the chiral surfaces states on both front, back and bottom surfaces are involved. Thus, these trajectories will contribute the transport for surface conductance $G_x^{(xz)}$, as plotted in Fig. S3(c).

Notably, the contribution of these trajectories to $G_x^{(xz)}$ can be quantitatively determined. Due to the chirality of these states, their transport properties can be simplified as a standard channel matching problem between the front/back and bottom surfaces in mesoscopic transport [1]. In specific, the $N \to \infty$ blue chiral channels on the bottom surface perfectly match with the $(L_z e^2/h - G_y^{(xy)})h/e^2$ red chiral channels on the front and back surfaces. Thus, the contribution of these backscattering routes to $G_x^{(xz)}$ equals $(L_z e^2/h - G_y^{(xy)})$. While $G_y^{(xy)}$ decreases by $(L_z e^2/h - G_y^{(xy)})$, $G_x^{(xz)}$ will increase by $(L_z e^2/h - G_y^{(xy)})$ accordingly, which preserves the relation:

$$G_x^{(xz)}+G_y^{(xy)} = [L_y e^2/h + (L_z e^2/h - G_y^{(xy)})] + G_y^{(xy)} = (L_y+L_z)e^2/h. \tag{S1}$$

Here, $L_y e^2/h$ is the intrinsic contribution of $G_x^{(xz)}$, which already exists for $t_c = 0$.

The disorder only tend to enhance the scattering between the chiral networks, which simply modifies the effective coupling t_c.

Supplementary Note 3: Kirchhoff's equation of Hall bar setups

current along y direction

In this section, we present the Kirchhoff's equation $\mathbf{I}_y = \mathbf{TV}$ of the Hall bar setup in Fig. S2(a). The sample sizes has been marked in the figure. For the six-terminal devices, the Kirchhoff's equation $\mathbf{I}_y = \mathbf{TV}$ can be rewritten as [1]:

$$\begin{pmatrix} T_1 & -T_{12} & -T_{13} & -T_{14} & -T_{15} & -T_{16} \\ -T_{21} & T_2 & -T_{23} & -T_{24} & -T_{25} & -T_{26} \\ -T_{31} & -T_{32} & T_3 & -T_{34} & -T_{35} & -T_{36} \\ -T_{41} & -T_{42} & -T_{43} & T_4 & -T_{45} & -T_{46} \\ -T_{51} & -T_{52} & -T_{53} & -T_{54} & T_5 & -T_{56} \\ -T_{61} & -T_{62} & -T_{63} & -T_{64} & -T_{65} & T_6 \end{pmatrix} \begin{pmatrix} V \\ V_2 \\ V_3 \\ -V \\ V_5 \\ V_6 \end{pmatrix} = \begin{pmatrix} I_y \\ 0 \\ 0 \\ -I_y \\ 0 \\ 0 \end{pmatrix}. \tag{S2}$$

V and $-V$ are the voltage potentials on the lead-1 and lead-4. V_n are the voltage potentials on the lead-n with $n \in [2,3,5,6]$. $I_y = I$ is the current between the lead-1 and lead-4 along the y direction. Here, one sets $T_n = \sum_{m\neq n} T_{n,m}$ with $T_{nm} = \mathrm{Tr}[\Gamma_n G^r \Gamma_m G^a]$ and $n, m \in [1,2,3,4,5,6]$. The retarded Green's function satisfies $G^r = [E + i\eta - \mathcal{H} - \sum_{n\in[1-6]} \Sigma_n]^{-1}$ for the six-terminal systems. Σ_n is the same as those in the two-terminal cases.

Noticing the transmission coefficient in Fig. S2(c), the Kirchhoff's equation for the quantized energy region with $E \in [-0.5t, -0.1t]$ can be simplified as:

$$\begin{pmatrix} T_1 & -T_{12} & 0 & 0 & 0 & 0 \\ 0 & T_2 & -T_{23} & 0 & 0 & -T_{26} \\ 0 & 0 & T_3 & -T_{34} & -T_{35} & 0 \\ 0 & 0 & 0 & T_4 & -T_{45} & 0 \\ 0 & 0 & -T_{53} & 0 & T_5 & -T_{56} \\ -T_{61} & -T_{62} & 0 & 0 & 0 & T_6 \end{pmatrix} \begin{pmatrix} V \\ V_2 \\ V_3 \\ -V \\ V_5 \\ V_6 \end{pmatrix} = \begin{pmatrix} I_\alpha \\ 0 \\ 0 \\ -I_\alpha \\ 0 \\ 0 \end{pmatrix}. \tag{S3}$$

Transmission coefficients marked in blue solid lines are set as zero since they are much smaller than the transmission coefficients marked in pink and cyan solid lines in Fig. S2(c).

Based on the chirality of the surface states, one should also notice the following relations should holds for the Chern vector protected quantized Hall conductances:

$$\begin{aligned} T_{62} = T_{26} = T_{35} = T_{53} \approx G_x^{(xz)} h/e^2, \\ T_{61} = T_{12} = T_{23} = T_{34} = T_{45} = T_{56} \approx G_y^{(xy)} h/e^2. \end{aligned} \tag{S4}$$

Here, G_x^{xy} (G_y^{yz}) is the two terminal conductance along x (y) directions contributed by the chiral surface states located on the x-z (x-y) boundaries. Considering $G_x^{(xz)} + G_y^{(xy)} = (mL_y + nL_z)e^2/h$, it illuminates the quantized $T_6 = \sum_{j\neq 6} T_{6,j} \approx T_{61} + T_{62} = mL_y + nL_z$, as shown in Fig. S2(b). Considering the restriction of the transmission coefficients, equation (S3) gives rise to

$$G_{yx} = I/(V_2 - V_6) = -(T_{61} + T_{62})e^2/h = -[G_x^{(xz)} + G_y^{(xy)}] = -(mL_y + nL_z)e^2/h. \tag{S5}$$

current along x direction

Generally, similar analysis for currents along the x direction as shown in Fig. S5. The Kirchhoff's equation $\mathbf{I}_x = \mathbf{TV}$ of Hall bar setup in Fig. S5(a) can be roughly simplified as:

$$\begin{pmatrix} T_1 & 0 & 0 & -T_{14} & 0 & -T_{16} \\ -T_{21} & T_2 & 0 & 0 & 0 & 0 \\ 0 & -T_{32} & T_3 & 0 & 0 & 0 \\ -T_{41} & 0 & -T_{43} & T_4 & 0 & 0 \\ 0 & 0 & 0 & -T_{54} & T_5 & 0 \\ 0 & 0 & 0 & 0 & -T_{65} & T_6 \end{pmatrix} \begin{pmatrix} V \\ V_2 \\ V_3 \\ -V \\ V_5 \\ V_6 \end{pmatrix} = \begin{pmatrix} I_x \\ 0 \\ 0 \\ -I_x \\ 0 \\ 0 \end{pmatrix}. \tag{S6}$$

Transmission coefficients marked in blue solid lines are set as zero since they are much smaller than the transmission coefficients marked in pink and cyan solid lines in Fig. S5(c) while sample size $L_y \to \infty$ and $L_z \to \infty$.

Based on the chirality of the surface states, one should also notice the following relations should holds for the Chern vector protected quantized Hall conductances:

$$\begin{aligned} &T_{14} = T_{41} \approx G_x^{(xz)} h/e^2, \\ &T_{16} = T_{21} = T_{32} = T_{43} = T_{54} = T_{65} \approx G_x^{(xy)} h/e^2. \end{aligned} \tag{S7}$$

Here, $G_x^{(xz)}$ ($G_x^{(xy)}$) is the two terminal conductance along x (x) directions contributed by the surface states located on the x-y (x-z) boundaries. Considering $G_x^{(xy)} + G_x^{(xz)} = mL_y + nL_z$, it illuminate the quantized $T_1 = \sum_{j\neq 1} T_{1,j} \approx T_{16} + T_{14} = mL_y + nL_z$, as shown in Fig. S5(b). Considering the restriction of the transmission coefficients, equation (S6) give rise to the quantized

$$G_{xy} = I/(V_2 - V_6) = (T_{16} + T_{14})e^2/h = G_x^{(xy)} + G_x^{(xz)} = (mL_y + nL_z)e^2/h. \tag{S8}$$

Supplementary Note 4: Disorder effects on the quantized Hall conductance

Fig. S6 shows the quantized Hall conductance versus the disorder strength [2]. The Anderson disorder $H_w = \varepsilon_n c_n^\dagger c_n$ with $\varepsilon_n \in [-W/2, W/2]$ is considered, and W is the disorder strength. The Chern vector protected quantized Hall conductance and the proposed relationships are robust against disorder, as plotted in Figs. S6(a)-(c). Further, the quantized G_{yx} is independent of the quantization of T_{61} or T_{62}. T_{61} and T_{62} for the Hall bar setups could deviate from their quantized values with $T_{61} + T_{62}$ still preserves its quantized value. These features are consistent with the proposed scheme for G_{yx}.

References

[1] Datta, S. *Electronic Transport in Mesoscopic Systems* (Cambridge University Press, Cambridge, England, 1995).

[2] Anderson, P. W. Absence of diffusion in certain random lattices. *Phys. Rev.* **109**, 1492–1505 (1958).

Supplementary Figure 1

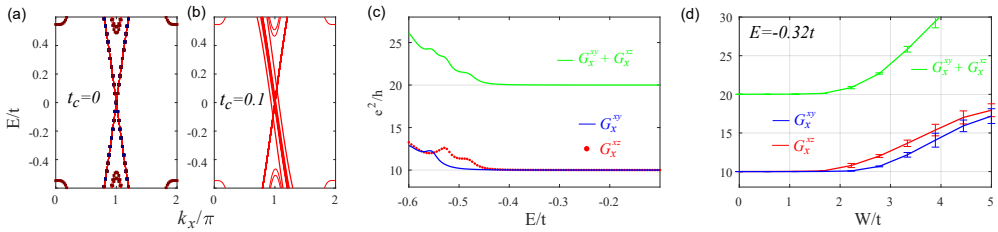

Figure S1: **Band structures and conductances.** (a)-(b) The band structures along the k_x. The sample sizes are $L_y = L_z = 10$ (c) and (d) The corresponding two-terminal conductances versus Fermi energy E and disorder strength W ,respectively. The sample sizes are fixed at $L_x = L_y = L_z = 10$, $N = 0$ with $t_c = 0.1t$.

Supplementary Figure 2

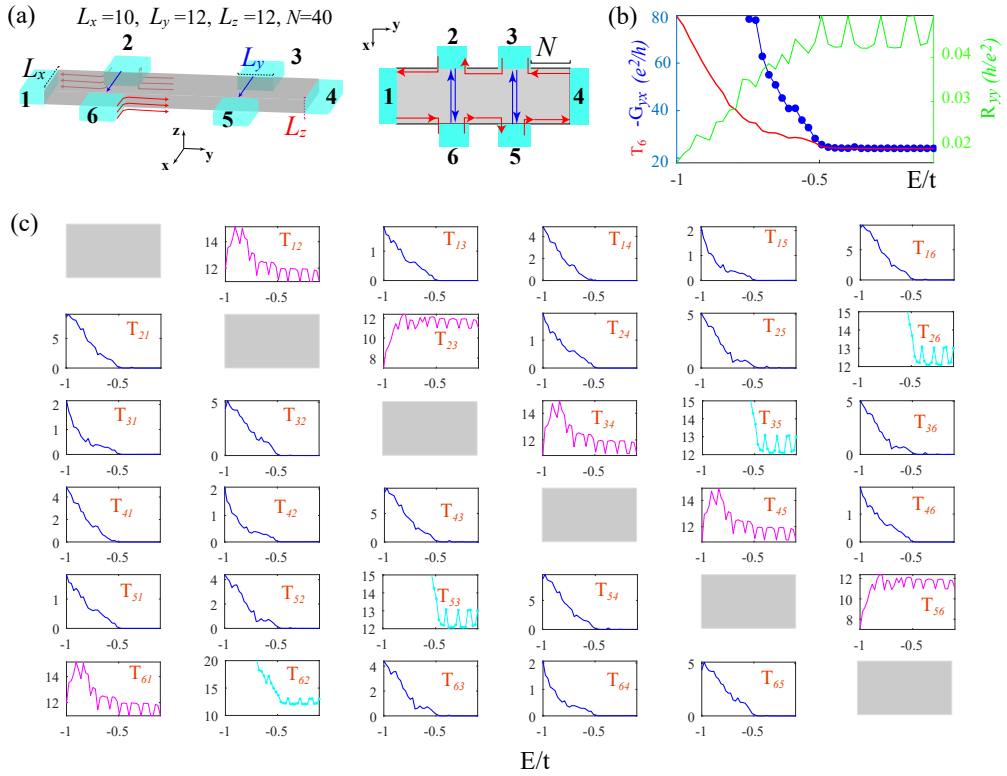

Figure S2: **Transmission coefficients of a Hall bar along the y-direction.** (a) The schematic plot of the Hall bar setup. The red and blue solid line with arrows represent the chiral surface states. The definition of sample sizes has been marked in the figure. The distances between different leads are set as $N = 40$. (b) The Hall $G_{yx} = I/(V_2 - V_6)$ (blue solid line), $T_6 = \sum_{j\neq 6} T_{6,j}$ (red solid line) and longitudinal resistance $(V_2 - V_3)/I$ (green solid line). (c) The transmission coefficients between different leads. The pink solid lines roughly present $T_{j,j+1} = T_{61} \sim G_y^{(xy)}$. The cyan solid lines roughly present $T_{62} \approx G_x^{(xz)}$. The extra transmission coefficients can be neglected for $E \in (-0.5t, -0.1t)$. In our calculation, we set $t_c = 0.1t$.

Supplementary Figure 3

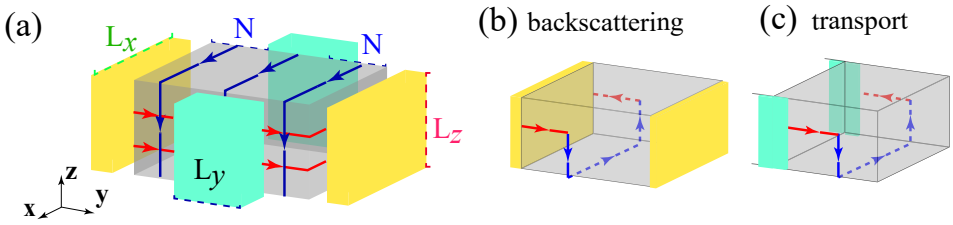

Figure S3: **Illustration of chiral modes and transport processes.** (a) Schematic distribution of the chiral surface states with Chern vector $\mathbf{C} = (0, 1, 1)$. The sample sizes has been marked in the figure. (b) and (c) present the influences of chiral networks for different leads.

Supplementary Figure 4

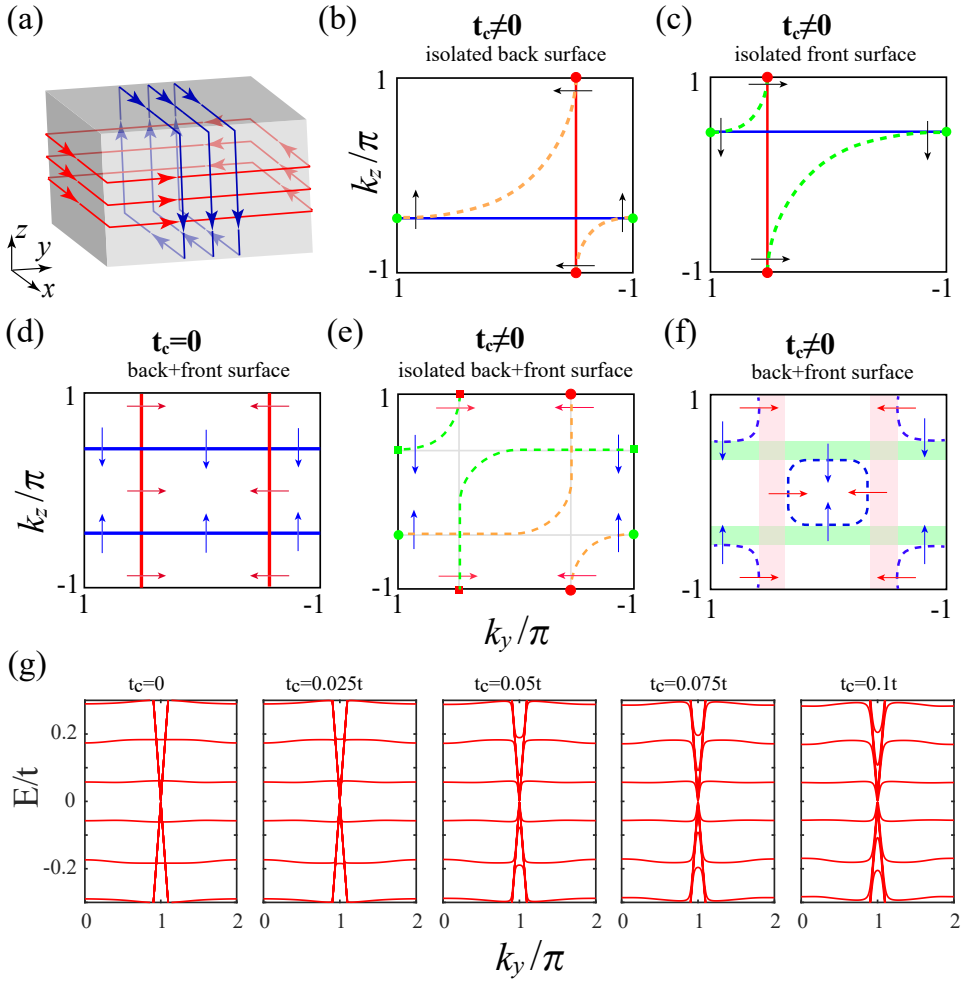

Figure S4: **Coupling between different chiral modes in momentum space.** (a) The schematic plot of the sample and the chiral surface states. (b)-(f) The schematic plot of the Fermi surfaces of the chiral surface states in the front and back (y-z) surfaces under different conditions. The blue and red solid lines are the Fermi surfaces for the red and blue chiral modes with $t_c = 0$. The arrows roughly mark the group velocity of the states. (g) The band structures E versus k_y for different t_c.

Supplementary Figure 5

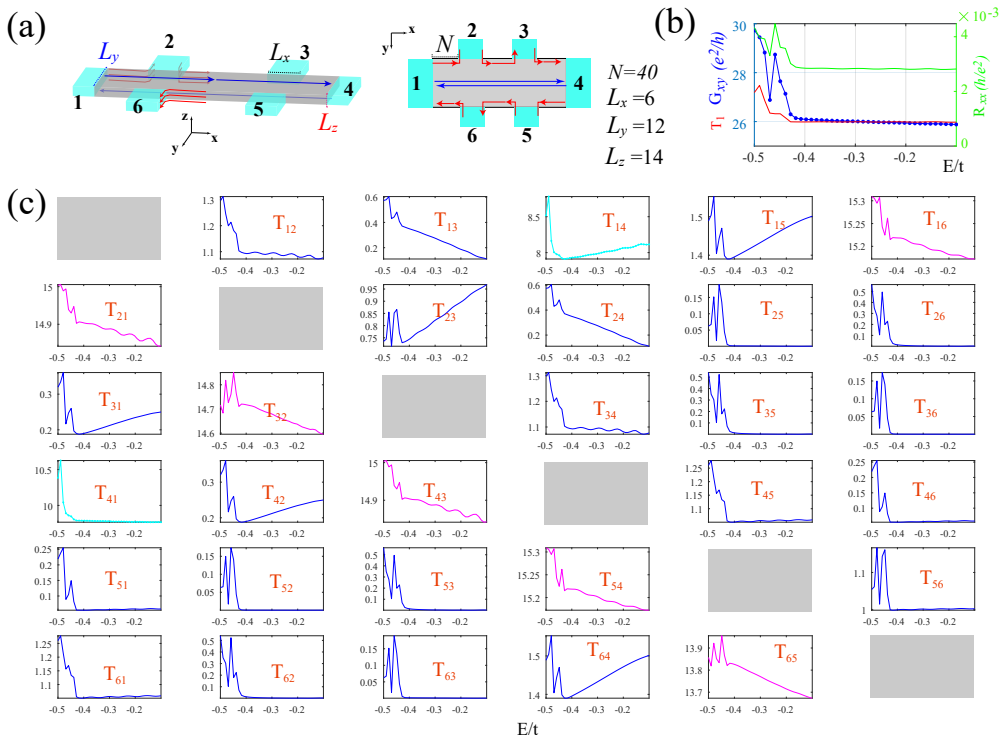

Figure S5: **Transmission coefficients of a Hall bar along the x-direction.** (a) The schematic plot of the Hall bar setup. The red and blue solid line with arrows represent the chiral surface states. The definition of sample sizes has been marked in the figure. The distances between different leads are set as $N = 40$. (b) The Hall $G_{xy} = I/(V_2 - V_6)$ (blue solid line), $T_1 = \sum_{j\neq 6} T_{1,j}$ (red solid line) and longitudinal resistance $(V_2 - V_3)/I$ (green solid line). (c) The transmission coefficients between different leads. The pink solid lines roughly present $T_{j+1,j} = T_{16} \sim G_x^{(xy)}$. The cyan solid lines roughly present $T_{14} \sim G_x^{(xz)}$. The extra transmission coefficients can be neglected for $E \in [-0.4t, -0.1t]$. In our calculation, we set $t_c = 0.1t$.

Supplementary Figure 6

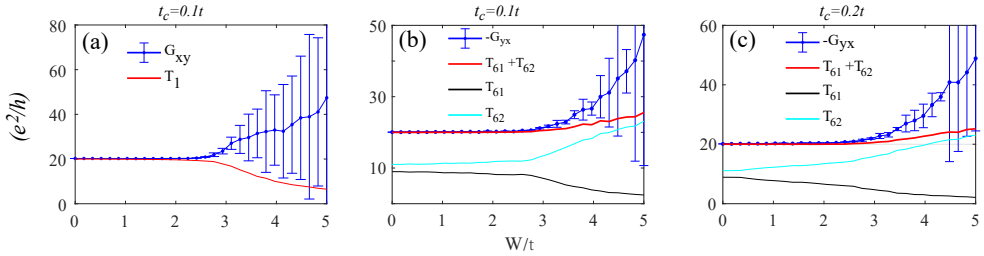

Figure S6: **Robustness of Hall conductance under disorder.** (a) and (b) The Hall conductance (blue solid line) and the response function (blue solid line) versus disorder strength W. The sample sizes are $L_x = L_y = L_z = 10$, $N = 40$ and $E = -0.2t$.